IEEE Access
Multidisciplinary ⋮ Rapid Review ⋮ Open Access Journal

Received June 18, 2021, accepted July 20, 2021, date of publication July 26, 2021, date of current version August 3, 2021.

Digital Object Identifier 10.1109/ACCESS.2021.3099428

Configurable High-Frequency Alternating Magnetic Field Generator for Nanomedical Magnetic Hyperthermia Applications

MICHAEL ZEINOUN[1,2], (Member, IEEE), DIEGO SERRANO[3], (Member, IEEE), PABLO TEZANOS MEDINA[1], ÓSCAR GARCÍA[3], (Member, IEEE), MIROSLAV VASIĆ[3], (Senior Member, IEEE), AND JOSÉ JAVIER SERRANO-OLMEDO[1,2]

[1]Center for Biomedical Technology (CTB), Universidad Politécnica de Madrid (UPM), Campus de Montegancedo, Pozuelo de Alarcón, 28223 Madrid, Spain
[2]CIBER de Bioingeniería, Biomateriales y Nanomedicina (CIBER-BBN), 28029 Madrid, Spain
[3]Centro de Electrónica Industrial, Universidad Politécnica de Madrid (UPM), 28006 Madrid, Spain

Corresponding author: Michael Zeinoun (michael.zeinoun@ctb.upm.es)

This work was supported in part by the Ministro de Ciencia, Innovación y Universidades through the Project Estudio de la eficacia de tecnologías alternativas de liberación de energía térmica y mecánica mediante nanoestructuras de óxido de hierro y de oro con aplicación en terapias anticancerígenas under Grant PGC2018-097531-B-I00.

ABSTRACT This article shows the use of a high-frequency Full-Bridge inverter to design an alternating magnetic field generator for experimental studies on anti-cancer treatment with magnetic nanoparticles. In magnetic hyperthermia, nanoparticles are used to raise the pathological cancerous cell's temperature high enough to induce their death by apoptosis, but not as high as to destroy them by thermal ablation of the whole tissue volume, consequently leaving healthy cells alive. Conventionally, sinusoidal alternating magnetic fields are used to heat the nanoparticles, which can be more easily produced than other waveforms. However, there are no theoretical nor experimental reasons to choose the sinusoidal waveform. This work aims to develop an improved power system to study the effect of different waveforms of the magnetic field on heat production when exciting magnetic nanoparticles, aiming at demonstrating that other waveforms can be much more efficient in producing heat than conventional sinusoids. To prove our hypothesis, we designed an inverter able to generate four waveforms at high frequencies and a fifth sinusoidal signal derived by a resonant capacitor, in the range of 100 kHz to 1 MHz and up to 10 mT of peak intensity. Also, we used SiC devices to process high currents at high switching frequencies efficiently. Additionally, to enhance the system efficiency, Zero-Voltage Switching is used to reduce switching losses and minimize electromagnetic noise and interference. The experimental results obtained with non-sinusoidal waveforms have shown a remarkable performance improvement compared to classical sine wave excitation. The nanoparticles' heat dissipation depends on the applied alternating magnetic field's signal slope, signal frequency, and peak field intensity. We conclude that further work deserves to be done to find the optimum work conditions in function of the used particle and biological environment to test if this type of magnetic field generator could overcome the conventional system's performance.

INDEX TERMS Hyperthermia, magnetic nanoparticles, DC-AC power converters, SiC, nanomedicine, alternating magnetic field.

I. INTRODUCTION

The global burden of cancer is estimated to have risen to 18.1 million new cases and 9.6 million deaths in 2018. One in 5 men /6 women worldwide develop cancer during their lifetime, and one in 8 men /11 women die from the disease [1]. With the increasing number of cancer cases every year, various treatments are being investigated to aid in the fight against this threat, especially nanomedical treatments, where nanoparticles are being used more and more in medical diagnostics and therapies. This article introduces the inverter used to experiment on a nanomedical cancer treatment technique named Magnetic Hyperthermia (MHT) based on alternating magnetic fields.

Magnetic Hyperthermia (or Hyperthermia with magnetic nanoparticles) is a modern method that aims to target cancer

The associate editor coordinating the review of this manuscript and approving it for publication was Gian Domenico Licciardo.

cells selectively, provided that the nanoparticles are successfully delivered to the targeted biological tissue, where their excitation will result in raising the environmental temperature to 43°C to 45°C, causing cancer cell damage due to their low resistance to heat [3], hence destroying cancer cells by apoptosis, leaving normal cells intact due to their high resistance to heat [4]. In experimental in-vitro set-ups, the Nanoparticles (NPs) are suspended in the same medium as the cancer cells. An external electromagnet is placed (see Fig. 1), where a high-frequency (usually between 100 kHz and 1 MHz) Alternating Magnetic Field (AMF) is generated (hence the need for a high-frequency AMF generator). The magnetic excitation results in the rotation of the nanoparticles and/or of their magnetic moment as well, resulting in heat generation (see Fig. 2). It is important to note that alternating magnetic fields at a frequency below 1 MHz and a magnetic field less than 1 T are considered harmless when exposed to biological tissues or processes [2]. This technique does not exceed these limits.

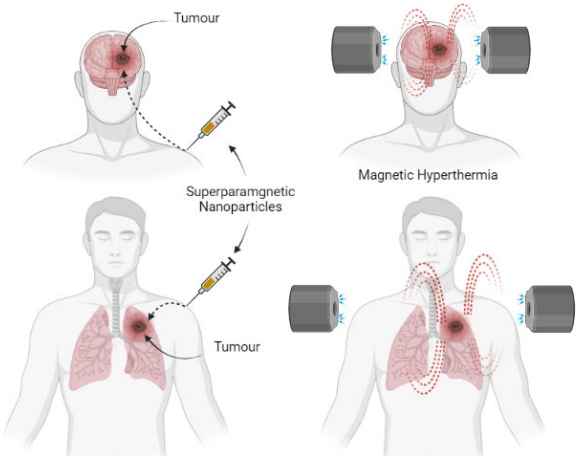

FIGURE 1. (Figure 1 changed) Particles are delivered inside the body and they reach the target tissue chemically driver. Afterward, the treatment with alternating magnetic fields can be applied to damage the tumor cells.

Currently, MHT is being used in various anti-cancer related studies, where it is also being used as a trigger to release therapeutic molecules due to temperature increase [6], like in the case of [8], where they used AMF and nanoparticles to trigger the drug-release using thermoresponsive matrices. [7] describes the current state and challenges of MHT, especially in nanoparticle reproduction. However, it also shows the new monitoring techniques that are being combined with MHT, like thermal imaging and magnetic particle imaging (MPI), which are vital since they allow us to monitor the distribution and heat dissipation from inside the cell.

Besides AMF, ultrasound and light have been used in thermal therapies, and drug release triggering [9], [10]. Ultrasound is used at high frequencies to ensure high penetration depth [11], damaging healthy tissues [9], while ultraviolet light suffers from low penetration depth.

Furthermore, magnetic nanoparticles (MNP), specifically iron oxide, which are the nanoparticles used in MHT, possess

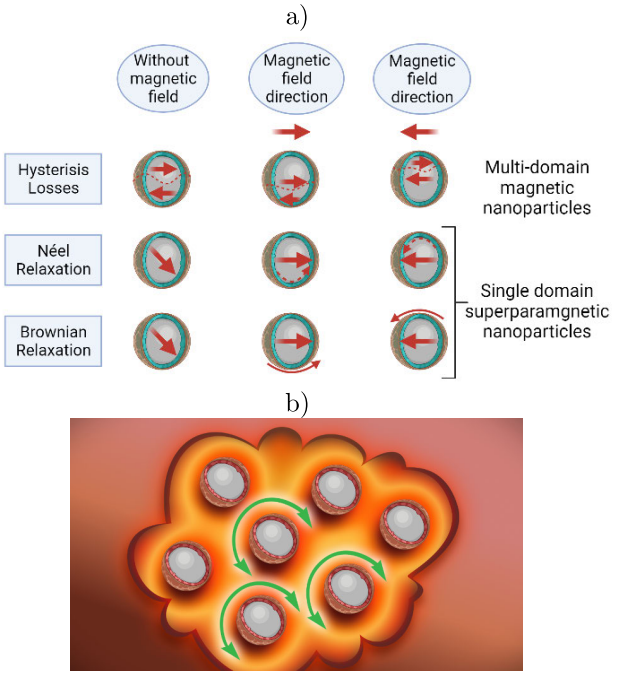

FIGURE 2. A. Different heat generation mechanisms of magnetic nanoparticles in response to a high-frequency AMF B. Nanoparticles heat generation representation inside the tumor.

high biocompatibility properties and are approved by the food and drug administration (FDA) [12] as magnetic resonance imaging contrast agents and heat mediator for either drug release triggering or cancer treatment using AMF [13], [14]. There are different sizes and shapes of Iron Oxide nanoparticles. The shape is categorized so that <10 nm are considered small nanoparticles, Néel Relaxation dominates their heating process; hence, it is frequency-dependent. On the other hand, particles larger than >10nm are regarded as large nanoparticles; their dominant heating process is Brownian Relaxation; hence, they are dependent on magnetic field strength [38]. These phenomena are represented in Fig.2 As for the shapes, there are various shapes of Iron Oxide nanoparticles, i.e., spherical, flower-shaped, etc. [19], [38]. In this study, the iron oxide magnetic nanoparticles that are employed have a diameter of 10.6 nm, having a standard deviation in the size of $\sigma = 3.5$, and a 75 mg/ml concentration, because they are expected to offer an excellent response in terms of thermal power dissipation [38].

When an AMF is applied to the NPs, they heat based on Néel and Brownian relaxation [3]. Commonly, Rosensweing's model is used to calculate the nanoparticles' heat dissipation following its excitation by a sinusoidal alternating magnetic field [40]. The power dissipation formula is expressed by:

$$P_{dissipated} = \pi \cdot \mu_0 \cdot \chi_0 \cdot H_{ac}^2 \cdot f \cdot \frac{2 \cdot \pi \cdot f \cdot \tau}{1 + (2 \cdot \pi \cdot f \cdot \tau)^2} \quad (1)$$

where μ_0 $(H \cdot m^{-1})$ is the vacuum permeability, χ_0 is the equilibrium susceptibility, f (s^{-1}) is the frequency, H_{ac} $(A \cdot m^{-1})$ is the amplitude of the magnetic field and τ (s) is the

relaxation time. However, the model was made for sinusoidal AMF signals, and no further models were developed using other waveforms.

It is essential to point out that all MHT experiments in the literature are conducted using sinusoidal AMF signals. To the best of the author's knowledge, there are no other available systems capable of providing different waveforms. However, these sinusoidal AMF face some limitations. In [15], MHT in Vivo problems emerged; the homogeneity of the heating inside the organ was highly dependent on the distribution of the NPs. Furthermore, MHT studies report that MNPs, once internalized in cells, show lower energy absorption per unit mass or specific absorption rate (SAR), ranging from 90 % to 50 % depending on particle size, shape, and composition [16], [17].

On the other hand, the aggregation effect was shown in [18], where the inefficiency of NPs to respond to AMF was observed due to the compaction of NPs as large aggregates with random NP orientation in lysosomes of tumor cells. In contrast, other studies attribute this effect to Brownian mobility restriction [17], [20]. Nevertheless, in [21] the decline in the effect of Brownian dynamics on NPs heating was studied; it was concluded that the magnetic moment of each constituent particle could sufficiently respond to the change in the magnetic field when the particle-field interaction is significantly more dominant, which leads to a larger area of the hysteresis loop, hence a better heat production performance. Therefore, a more considerable efficacy in producing heat could solve most of the above-described problems, either improving the nanoparticles' behavior, which is the line of research followed by most scientific community, or improving energy delivery from the exciting magnetic field, which is the main aim of this work.

Our background hypothesis follows that the most effective heat production occurs during the transients phase (which refers to the transitional phase of the AMF signal when it is changing its polarity), where the particle magnetization changes, and physical miss-orientation relative to the field direction are more considerable. Transients take place mainly around the zeros of the magnetic field. The particle magnetization (that follows the exciting field almost without memory effect since they are superparamagnetic) is high around the field peaks, so the particle strongly tends to stay oriented in the direction of the exciting field without producing further heat dissipation. On the contrary, when the magnetic field is changing, the dissipation would be much higher. Instead of reaching a steady-state in magnetic momentum and particle rotation, the heat dissipation could be considered a series of transients taking place around the zeros. Thus, high magnetic field peak values would not be as useful as sharp slopes when the field changes its direction in its zeros to dissipate energy as heat. The optimum sharpness needed could depend on the experimental conditions. Since sinusoidal waveforms slope and peak value are dependent on each other, it is impossible to clarify this hypothesis. There is no commercially available system capable of producing alternating magnetic fields of enough intensity within the frequency range of interest other than following sinusoidal waveforms. And, although we can theoretically increase the efficiency of the sinusoidal waveform by increasing its magnetic field intensity and/or frequency, we must consider the risks of biological damage to the patient due to induction phenomena in the tissues [44]–[47]. Hence, there is a limit for the operating magnetic field intensities and frequencies, making it vital to seek new waveforms able to reach similar efficiencies while requiring lower intensities and frequencies.

In our first attempt [22] of using non-sinusoidal waveform, with non-coupled slopes and peak intensities, we observed that the heat production does not follow the rule (1) for low magnetic intensities. On the contrary, the heat production is higher than expected, pointing to a more relevance of the slopes over the peaks for heat production. In our second attempt [23], [24], with a better prototype, we could demonstrate that, contrary to the conventional rule (1) the frequency is not enough to define the heat production; all the rest of the variables kept equal. Furthermore, with just square signals of changing duty cycles, it is possible to change the heat production, again pointing to the transients around the zeros as the leading cause of heat dissipation. However, in both attempts, the developed devices had severe technical issues. The instrument used in the first attempt was a signal amplifier used for antennas, which unfortunately, taught us that only sinusoidal waveform could be amplified. In contrast, the rest of the waveforms were generated with severe distortion. The device used in the second attempt was much better than the previous one, yet it still lacked significant measures to make it reliable. As a result, it suffered from constant component overheating and malfunctioning. Therefore, in this paper, we present the last prototype with which we have gained a much larger control on the variables to produce signals with slopes, peak intensities, and frequency decoupled, including a sinusoidal waveform for the sake of comparison with the conventional case of magnetic hyperthermia with nanoparticles, again, all the rest of variables kept unaltered among different experiments. Also, better layout practices and safety measures were taken while designing this device to ensure a more stable performance during the experiments, allowing it to withstand the generation of high-current AC output at high frequencies and for an extended period without any component overheating issues.

Rosensweig connected the magnetic field to the ΔT in NPs [40]. However, our previous results [22]–[24] showed that the type of the AMF signal, signal frequency, and even particle size (tiny particles $<$10 nm) conditions the proportionality between ΔT and B.

This paper shows the design and experimental validation of an AMF device based on a full-bridge inverter to study the effect that different shapes for the magnetic field have on iron oxide superparamagnetic nanoparticles (SPION) heat dissipation. We aim to prove that the AMF signal's slope increases the NPs heating efficiency and that unconventional signals

contribute more to magnetic hyperthermia than conventional sinusoidal signals.

The paper is organized as follows. Section II will discuss the prototype design, explaining design features, the control chip used, and the device selection. Next, Section III will describe the experimental protocols and the measurement method. Finally, Section IV includes the device characterization, AMF output waveforms, and experimental results.

II. INVERTER FOR MAGNETIC HYPERTHERMIA

This section will discuss the inverter's essential design details that drive the air coil where the sample is placed and disposed to a high-frequency magnetic field.

First, the specifications for the MHT device are covered. It has to generate four unconventional signals with different slope angles, namely: Square-to-Trapezoidal, Trapezoidal, Triangular-to-Trapezoidal, and Triangular, at several frequencies going from 100 kHz to 1 MHz in 100 kHz steps. Also, a sinusoidal signal is derived for comparison with the conventional method. The inverter has to generate a peak load current of 100 A_{pk-pk}. However, this value is not achievable in all the experiments because, at high frequency and the selected inductance, the input voltage must be high as well, thus limiting the coil current. This phenomenon will be discussed in Section II-A.

The load used in this work is an air coil made of a single-strand wire consisting of 30 wires of 0.55 mm radius each. It has 14 turns, 5.5 cm height, and an internal and external radius of 2.85 and 3.25 cm, respectively. The coil is described in detail and optimized in [23]. The NPs used, and their characteristics are described in the previous section.

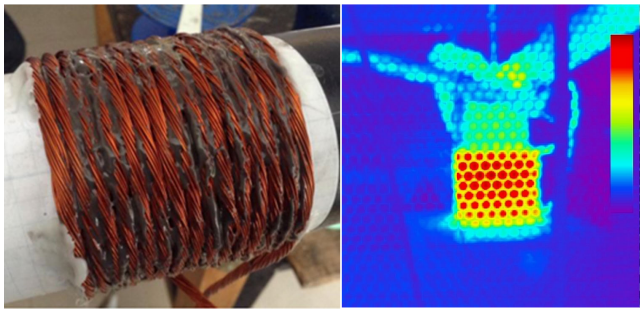

FIGURE 3. a) The air coil used in this study after while being manufactured in [23] b) Thermal photo of the coil while operating during a hyperthermia inert experiment.

Since the goal is to generate waveforms other than sinusoidal signals, conventional AMF devices are not applicable. It is difficult to find in the literature the devices used by researchers to perform their hyperthermia test as they are often published in biology-related magazines where the deceive itself is not of interest. Some AMF generators are available in the market, like the CELES MP Generator (Five Celes, Lautenbach, France). However, they are designed to produce exclusively conventional sinusoidal signals from 50 kHz to 400 kHz, in addition to their financial requirement. Which is why we developed our own device.

The conventional current generation methods into coils are based on radio frequency (RF) power amplifiers or waveform amplifiers, as in [35] or [36] respectively. RF amplifiers can reach a very high bandwidths, but they are lossy, bulky, expensive, and are limited to low currents. For instance, a class-B amplifier generating a sinewave for an inductive load would have a power loss given by $P_{loss} = V_{in} \cdot I_{pk-pk}/\pi$, where I_{pk-pk} is the peak to peak current of the sinewave and V_{in} the input voltage (positive or negative). Considering $V_{in} = \pm 100$ V with the load referred to the midpoint, to obtain 20 A_{pk-pk}, the losses would be 637 W.

Another common solution is to use a Full-Bridge with a capacitor in series with the load switched at the resonant frequency, commonly found in induction heating devices. In [25], an inverter is also used to develop an AMF generator using a Full-Bridge with Zero-Current Switching (ZCS). Due to the resonance of the inductive load with the resonant capacitor, relatively low voltages can be used to obtain high current. As a result, low voltage devices can be employed. The advantage of such solution is the simplicity of the design and that much lower losses are achieved compared to power amplifiers. However, this solution is only valid for sinusoidal excitation, at a single frequency. As the frequency is changed, the capacitor must be changed as well.

Also, there are solutions based on multicell converters. For example in [41] and [42] multicell converters were designed to be used in pulsed electroplating anti-cancer treatment applications. However, due to the complexity of these designs, they cannot be justified very well; hence we chose to move towards simpler designs.

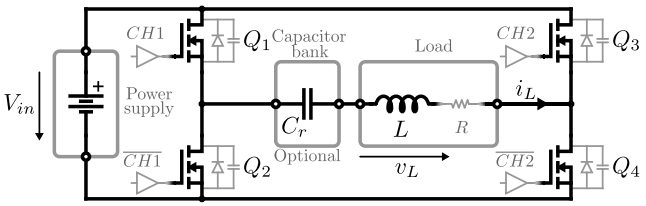

FIGURE 4. Schematic of the full-bridge inverter.

A. OPERATION OF THE INVERTER

The inverter designed in this work has the structure shown in Fig. 4, composed of 4 SiC MOSFETs, the load, the input power supply, and an additional resonant capacitor that is added only for sinewave signals.

The primary objective is to generate an AC output current, allowing the user to configure its amplitude, frequency, and shape. Controlling both legs, the shape of the AC current in the load can be adjusted, and the DC voltage of the power supply controls the amplitude of the inverter's output current.

The different shapes for the load current can be obtained with conventional phase-shift control. A constant duty cycle of 50% is used for each leg, switching at the same frequency as the target output shape. Changing the phase-shift (ϕ) from

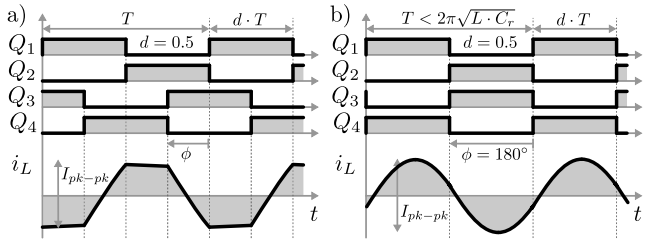

FIGURE 5. Inductive load output signal generation. a) for piecewise functions, at 90° phase-shift in the example b) for sinusoidal signals, adding C_r.

Q_1 to Q_3 from 0° to 180° controls the shape of the current waveform as shown in Fig. 5 a). When the phase-shift is $\phi = 180°$, the waveform is triangular. When it is 90°, it is trapezoidal. And, as it gets closer to 0°, the squarer the signal becomes. In this work, ϕ takes the values 180°, 135°, 90° and 45° for the Triangular, Triangular-Trapezoidal, Trapezoidal, and Trapezoidal-Square, respectively.

Then, the amplitude is controlled with the input voltage. The relation between the input voltage, V_{in} and the peak to peak current in the inductor I_{pk-pk}, is given by (2) if losses are neglected.

$$I_{pk-pk} = \frac{V_{in}}{L} \frac{\phi}{180°} \frac{T}{2} \tag{2}$$

From this equation, it is clear that the highest input voltage is reached when the waveform tends to be a square and the switching frequency is increased. For instance, in the case of the almost square signal (Trapezoidal-Square), which has the most significant phase-shift value between the 4 generated signals ($\phi = 45°$), and for an inductance of 10 μH, the required input voltage to reach 60 A_{pk-pk} at 100 kHz is 480 V. In contrast, at 1 MHz, 4800 V is needed to achieve the same output current value. Since our power supply is limited to 500 V, we are only able to generate 7.5 A_{pk-pk} in the latter case.

To obtain sinusoidal shapes, a resonant capacitor is added in series with the load, as in [25]. A large current can be obtained even with relatively low input voltage values if the switching frequency is selected near the resonant frequency of the resonant tank formed by the load and the additional capacitor. The same driving signal as for the triangular shape is used, as shown in Fig, 5 b). Moreover, Zero-Voltage Switching (ZVS) can be obtained if the switching frequency is above the resonant frequency, as discussed next.

One advantage of the Full-Bridge with phase-shift modulation is that ZVS can be achieved in all switches using the inductive load current, reducing switching losses [31].

For ZVS, the inductor current has to discharge the parasitic capacitance of the MOSFET, C_{oss}, that is going to be turned on during the dead time between the signals Q_1 and Q_2, and between Q_3 and Q_4. This is only possible if the dead time is long enough and the inductor current is high enough. For the piecewise functions, the current in any transition is directly given by $I_{pk-pk}/2$ (2). A reasonable approximation for the minimum dead time for ZVS is given in (3) when the current in the transition is high enough, this is, when (4) is met [37].

$$T_{dead\ min} = \frac{4 \cdot Q_{oss}|_{V_{in}}}{I_{pk-pk}} \tag{3}$$

$$L \cdot \frac{I_{pk-pk}^2}{4} \gg 2 \cdot Q_{oss}|_{V_{in}} \cdot V_{in} \tag{4}$$

Using the Q_{oss} at V_{in} reasonably accounts for the effect of the dependency of C_{oss} with v_{ds}, based on [37]. A more accurate model that accounts for the evolution of the inductor current in the dead time is out of the scope of this paper.

This limit is harder to meet at a maximum frequency or lower phase shift. Similarly, at low input voltage, as $Q_{oss}|_{V_{in}}$ is commonly steeper, the ZVS condition is more challenging to meet due to the low current. The minimum current to be tested is $I_{pk-pk} = 5$ A, for Trapezoidal-Square at 1 MHz. For this test, V_{in} is equal to 400 V and $Q_{oss}|_{400\ V} \approx 250$ nC. In this case, applying (4) ZVS cannot be achieved. ZVS imposes an additional limitation to the tests that can be performed, as the tests performed without ZVS generate too much noise due to the high dv/dt that impairs the measurements.

For the Sinewave signal, ZVS is simply obtained by selecting $f_{sw} > f_r$ to ensure that the transition is done with enough current in the inductor.

For this application, GaN or SiC devices are preferred due to the high switching frequency operation, and the high current [43]. However, since the maximum voltage is 500 V, using 650 V GaN devices is not safe due to the ringing in the drain-source voltage. Therefore, 1200 V SiC devices are selected for this inverter. The use of Full-Bridge inverter switching at such high frequency (1 MHz) is only possible thanks to the use of SiC devices due to their reduced $R_{dson} \cdot Q_g$ figure of merit [32], which enables fast switching transitions and low conduction losses at the same time. The selected SiC MOSFET is the *Cree C3M0016120K*, rated to 1200 V and 115 A. It is driven with the *SI8233BB* isolated driver. A DC bus with a capacitor bank was placed tightly close to the MOSFETs, to avoid voltage ringing [33]. Also, to prevent ringing in the gate, ferrite beads were used as gate resistors [34]. They proved effective at eliminating parasitic oscillation while minimizing switching losses because they act like frequency-dependent gate resistors. To supply the gate drivers, 3 separated 12 V power supplies are used, one for each high-side MOSFET and one for both low-side MOSFETs. Common-mode chokes are used in the supply to avoid common-mode current at switching frequency due to the external power supply's parasitic capacitance to ground. Also, a Schottky diode was placed in parallel with the gate resistor of 3 Ω to provide a strong pull down to avoid spurious turn-on when the complementary switch is closed. Finally, a Faraday cage was placed around the MHT device case to ground any electromagnetic waves generated by the circuit. A picture of the inverter is shown in Fig. 6.

B. CONTROL CARD AND INTERFACE

To generate the driving signals, the *STM32-F446RE* control card is employed. It has an *Advanced Timer* that can operate in

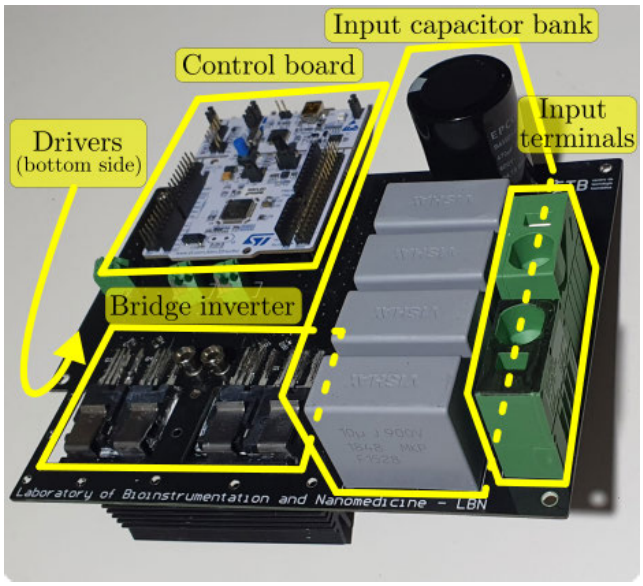

FIGURE 6. Prototype picture highlighting the different parts of the circuit.

Toggle Mode, which generates signals at 50% duty cycle at all times, having to only phase-shift the pulses from 0° to 180° to acquire all the five signals listed in the previous section. As mentioned earlier, the current amplitude is controlled by the DC power supply; however, the signal's shape and frequency are configured by software. The *Nucleo-F446RE* has a clock speed of 180 MHz, which is more than enough for this application since the highest switching frequency is 1MHz. As for the gate pulses generation, although the circuit consists of 4 MOSFETs requiring 4 gate inputs, it was unnecessary to program all 4 *STM32-F446RE* output channels. Instead, we set only 2 channels to generate the desired pulses. In contrast, the other two were easily obtained as the *STM32-F446RE* provides every channel with an inverse channel. That way, a channel is connected to the high-side MOSFET and its inverse to the low-side MOSFET. Furthermore, the *STM32-F446RE* allows us to introduce a dead-time between the main channel and its inverse. As a result, only the high side switches are controlled, namely *CH1* and *CH2* (see Fig. 4). The Nucleo generates 3.3 V pulses that go into isolated gate drivers. A TTL serial was added due to the high noise, to isolate the Nucleo from the PC (see Fig. 7).

A small current transformer was added in series with the load to calculate the magnetic field flux based on the current in the coil. The current is obtained by measuring the voltage across a shunt resistor in the secondary side of the transformer. With the selected values, the obtained gain is 0.1 V/A. $\vec{B}$, on the other hand, is estimated using the Bio-Savart formula, which in the case of our coil at $z = 0$ is calculated by:

$$\vec{B}(t) = \frac{\mu \cdot I(t) \cdot N}{2 \cdot (r_2 - r_1)} \ln \frac{r_2 + \sqrt{(l/2)^2 + r_2^2}}{r_1 + \sqrt{(l/2)^2 + r_1^2}}. \quad (5)$$

where the magnetic permeability is $\mu = \mu_0 = 4\pi \cdot 10^{-7}\, H/m$ since the coil is air core, N is the number of turns, r_2, and r_1 are the outer and inner radius of the coil, respectively, and l is the length of the coil.

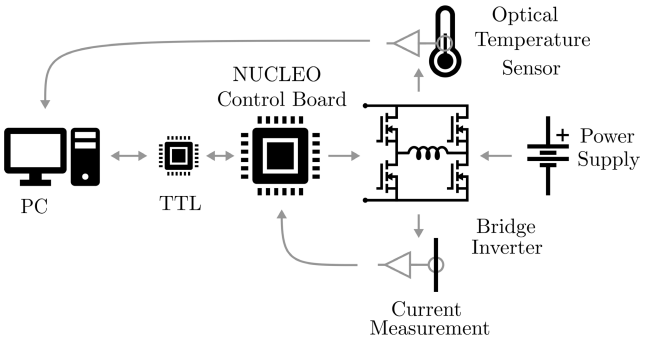

FIGURE 7. Magnetic hyperthermia connection diagram.

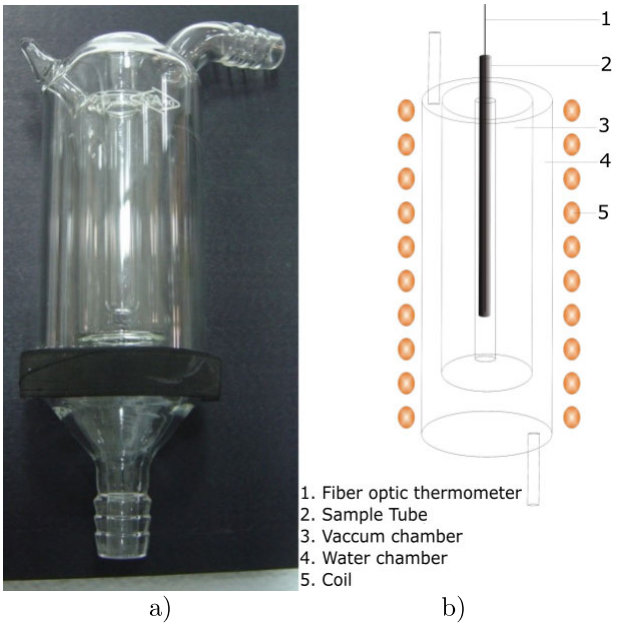

FIGURE 8. a) The sample holder b) Detailed drawing of the sample holder's layers.

However, to determine the validity of (5), a simulation in *Ansys Maxwell* was conducted in [23]. First, we introduced the same current values used in the simulation. Then, we compared the calculated $\vec{B}$ to the one acquired by the simulation. Both values were almost identical, which means the formula is valid.

III. EXPERIMENTAL SETUP

The purpose of this study is the measurement and analysis of the temperature curves of the NPs, for which a rigorous experimental protocol was developed. We have set a globalized initial condition for all the samples used in all experiments to make a valid comparison of the maximum temperature reached.

Fig. 9 shows the entire setup, which is divided into 2 parts: The electronics part and the experimental part.

The electronics part consists of the high-frequency AMF, which is placed inside a box designed by a 3D imprinter

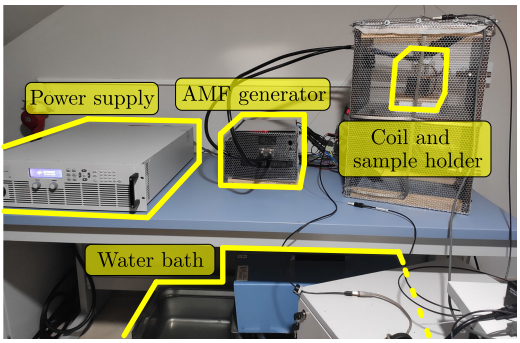

FIGURE 9. Hyperthermia set-up.

covered in Faraday cage and a RF plate on the top. Next to it we have the 500 V/60 A power supply on one side and the inductor coil placed inside a second Faraday cage. The experimental part, on the other hand, consists of the sample itself, which is placed inside a sample holder (see Fig. 8; described thoroughly in [23] and [22], divided into 3 layers:

- Sample in the middle.
- Vacuumed layer that surrounds the sample.
- Water layer that surrounds the vacuumed layer connected to a pump by tubes and through which 37°C water is continuously pumped.

The purpose of the continuous flow of water at a constant temperature is the total thermal isolation of the sample to forbid any external heat to affect the temperature measurement, especially the heat generated by the losses in the coil. Then, we have the *Luxetron* fiber optic temperature measurement tool, which is connected to the user computer via a *LabView* platform. In addition, an ultrasonic bath is available, which is used before every experiment to neutralize any present aggregation in the sample.

Hence, the experimental protocol goes as follows:

-First, a 500 μl sample containing the nanoparticles is placed inside a 177.8 mm $\times$ 5 mm tube. Next, the tube is placed for 90 seconds in the ultrasonic bath, set at 37°C, to neutralize any aggregation that might have occurred. Afterward, the sample is placed in the sample holder found in the Faraday cage. The sample must coincide at the very middle of the coil (defined as $z = 0$), which is why the sample holder and coil's initial position are fixed accordingly.

-Although the external temperature is isolated from the sample, the water temperature continuously going through the sample holder affects the sample's temperature, which is set at 37°C to represent the temperature of the human body. Therefore, after placing the sample inside the holder, the temperature will be stabilized at 37°C. This procedure is done in all the experiments; hence, creating almost the same initial condition and initial temperature.

-Meanwhile, three fiber optic cables are placed at three different measuring points:

- The first measures the ambient temperature through a cup of water at room temperature.
- The second measures the temperature of the part of the tube found outside the sample holder's chamber.
- The third is for the NPs sample's temperature measurement.

However, it is essential to point out that the temperature should be recorded at the $z = 0$ point of the sample. Since the cables have a curved end, a Pasteur transfer pipette is used, through which the fiber optic is introduced, and only a few millimeters of the tip of the cable meets the sample. Initially, the 177.8 mm $\times$ 5 mm tube is cut short by a diamond head pen so that the Pasteur pipette's tip, hence the fiber optic's tip, is at $z = 0$ of the sample.

-Once the fiber optics measures the sample temperature at 37°C, the required voltage on the DC power supply is set to reach the desired peak-to-peak AC load current, which is measured by a current probe connected to an oscilloscope, allowing us to visualize the shape and amplitude of the current. High-power RF cables were used to connect the inverter output to the load to reduce electromagnetic interference produced by the AC output passing through the load.

-During the 15 mins, the fiber optic temperature measurement is sampled every 1 second, and only the last measured value is used after the 900-second mark is reached.

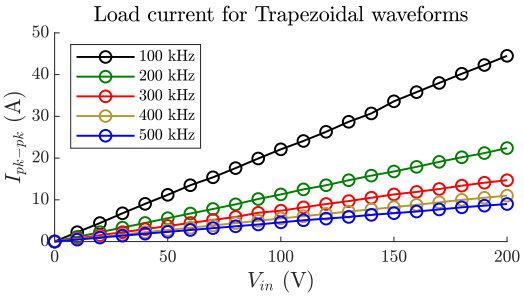

FIGURE 10. Trapezoidal signal characterization curve.

IV. RESULTS

After ensuring that all devices functioned correctly, the inverter was tested.

A. DEVICE CHARACTERIZATION

First, the theoretical values acquired from the relationship between V_{in} and I_{pk-pk} in (2) had to be compared to the measured values. The measured values were slightly different from the calculated values due to RF cables, which increased the inductance of the load, resulting in a slightly higher voltage requirement than the theoretical value to reach a certain current amplitude. The results are shown in Fig. 10. Then, applying the I_{pk-pk} values in (5) the magnetic field is calculated for every given current. As for the output signals, they are represented in Fig. 11 and Fig. 12.

At high frequencies, the losses are high because of the high input voltage required to obtain the desired magnetic field strength. Similarly, the phase-shift is also proportional to the current, and a higher voltage is needed when the phase shift is increased, as given by (2).

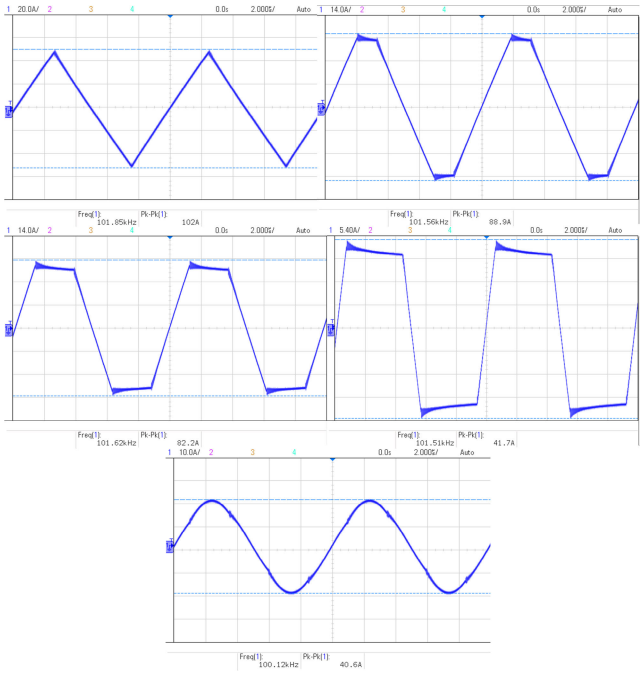

FIGURE 11. Load current at 100 kHz for triangular, trap-triangular, trapezoidal, trap-square and sinusoidal signals at 101 A_{pk-pk}, 88.9 A_{pk-pk}, 82.8 A_{pk-pk}, 41.7 A_{pk-pk} and 60 A_{pk-pk} respectively.

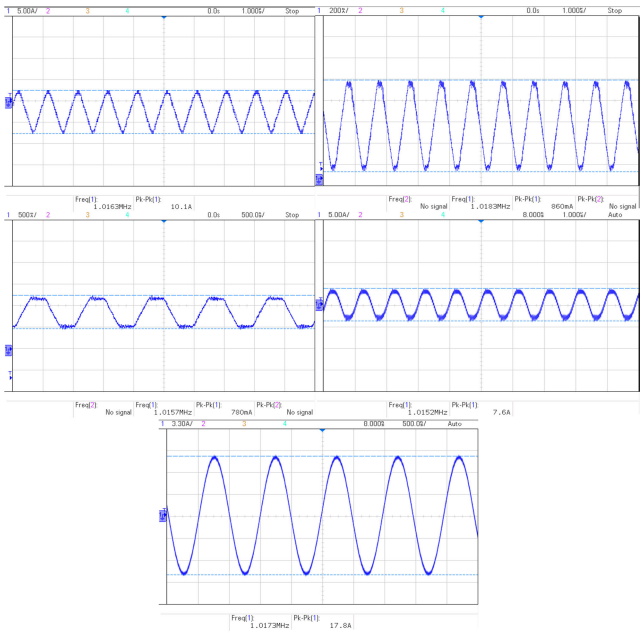

FIGURE 12. Load current at 1 MHz for triangular, trap-triangular, trapezoidal, trap-square and sinusoidal signals at 10.1 A_{pk-pk}, 0.860 A_{pk-pk}, 0.780 A_{pk-pk}, 7.6 A_{pk-pk} and 17.8 A_{pk-pk} respectively.

B. VALIDATION EXPERIMENTS

The first experiment was conducted to ensure the sample was isolated from external temperature, especially coil heating. Hence, de-ionized water (also known as MiliQ water) was placed in the sample, and various tests were conducted. For example, Fig. 13 shows the results under a sinusoidal signal

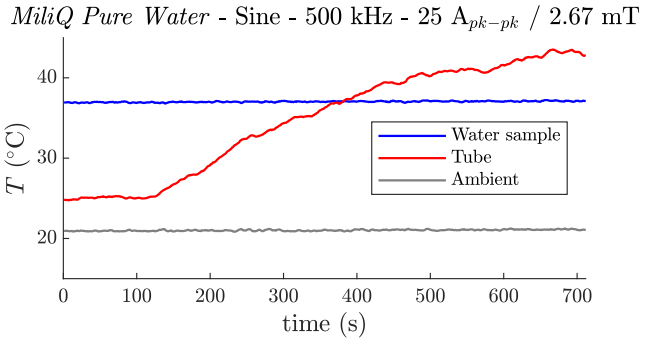

FIGURE 13. Sample temperature isolation test using de-ionized water.

25 A_{pk-pk} at 500 kH. The gray curve represents the ambient temperature, whereas the orange curve represents the Pasteur pipette temperature outside the sample holder, hence affected by external heat interference. The Fig. 13 was chosen to show that due to the overheating of the solenoid coil, the Pasteur pipette temperature raised to around 43°C. However, the blue curve that represents the sample temperature stayed in both cases steady at 37°C, proving that whatever is placed inside the sample holder is totally isolated from external interference.

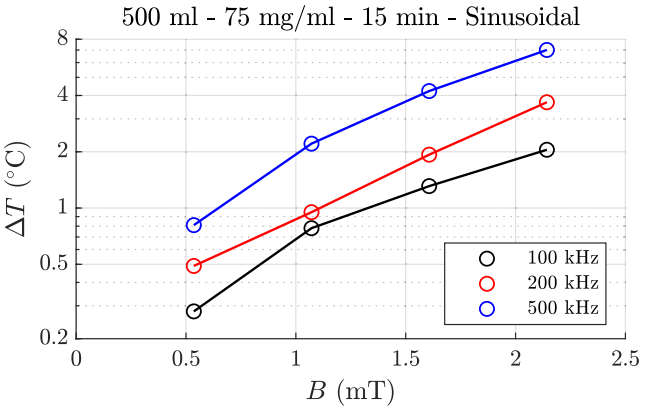

FIGURE 14. Heating experiments with sinusoidal signal at 100 kHz, 200 kHz and 500 kHz for different magnetic field intensities.

Now that we are sure that the sample is isolated and that any heat generated is due to hyperthermia, a series of experiments are conducted. It is important to note that all experiments were performed using the same nanoparticle, a 10 nm Iron-Oxide non-biofunctionalized nanoparticle, at a volume of 500 μl, at a concentration of 75 mg/ml. The duration of all tests is set to 15 minutes. First, the effect of the frequency on the nanoparticle's heating was tested using the conventional sinusoidal signals at 3 different frequencies, 100 kHz, 200 kHz, and 500 kHz, at different magnetic field strengths. The results are shown in Fig. 14 and imply that a higher temperature was reached at high frequencies for the same magnetic field intensity. This result proves that the power dissipation of the nanoparticles is proportional to the AMF frequency and increases with increasing magnetic field strength.

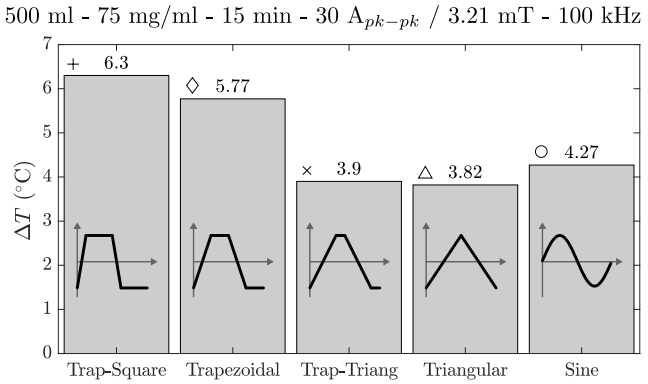

FIGURE 15. Slope efficiency experiments results at 100 kHz and 3.21 mT.

Next, the effect of the slope of the signal was tested by fixing the frequency of the signal at 100 kHz and the magnetic intensity at 3.21 mT and varying the signal; hence, varying the slope of the AMF waveform. The results in Fig. 15 show that the highest heating efficiency is reached using the trapezoidal-square signal, which is the signal with the highest slope value, followed by the trapezoidal signal. The sinusoidal signal reached a lower heating value than the previous signals. It marked a higher value than the Trapezoidal-Triangular and triangular signs, respectively, the latter being the signal with the smallest slope value. These measurements prove that the nanoparticles' power dissipation depends on the slope of the AMF signal. The slopes and frequency effects were studied at 3 different frequencies for various magnetic field values to validate the previous conclusions further. The results are shown in Fig. 16.

The Trap-square signal's efficiency is superior throughout all the magnetic field intensities and frequencies, always followed by the Trapezoidal signal, except at 100 kHz/1.07 mT, where the former scored a lower value than expected compared to the latter and sinusoidal signal. It is essential to point out that these experiments were repeated three times to ensure that the data is correct, and all the results were in a 0.05°C range. Further investigations are being made to determine if it is a particular case or a specific pattern for this unusual phenomenon.

Nevertheless, at 2.14 mT, the desired results were acquired. The conventional sinusoidal at 0.53 mT and 1.07 mT is found behind Trap-Square and Trapezoidal signals; however, at 2.14 mT, it is surpassed by Trapezoidal-Triangular signal at 200 and 500 kHz. The Triangular signal is the least effective in all frequencies and magnetic field intensities. Unfortunately, at 500 kHz, due to extreme coil heating, for the moment, the experiments were limited to 1.07 mT in the case of Trapezoidal and 0.53 mT in the case of Trapezoidal-Square. Once a better coil is developed, experiments at high frequencies and amplitudes will be explored.

The results prove that a considerable increase in heat generation can be obtained with waveforms different from conventional sinewaves. Nevertheless, the relation between heat generation and the time-varying magnetic field must be

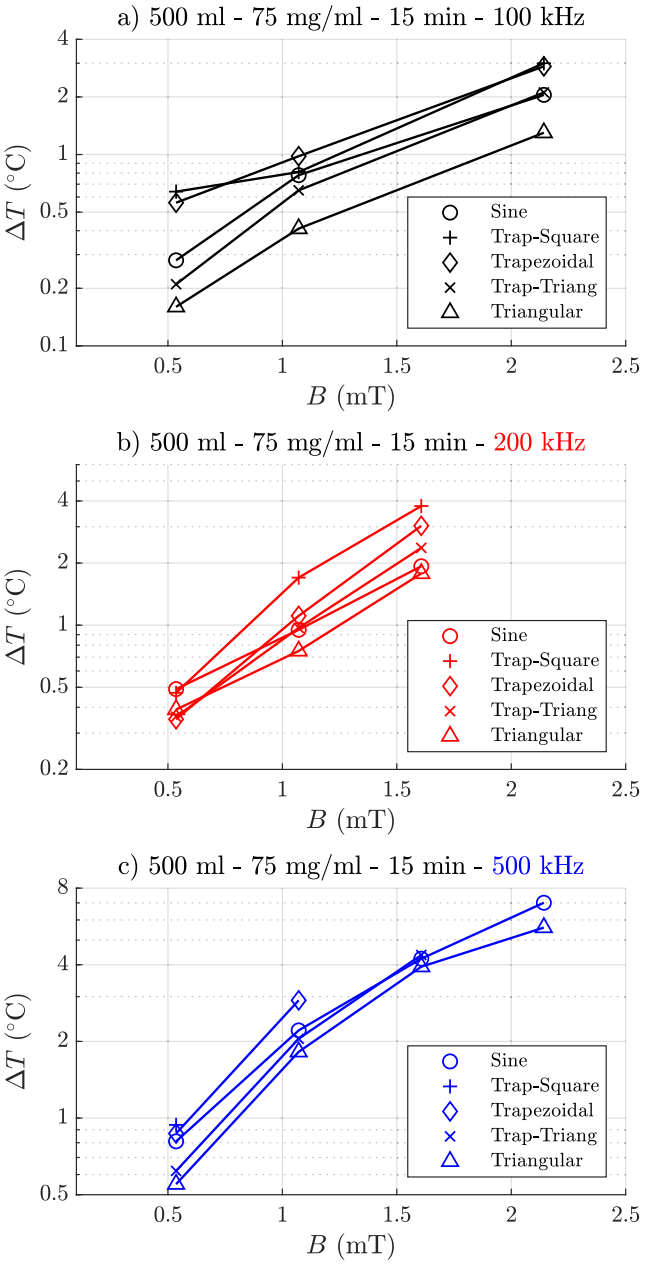

FIGURE 16. Hyperthermia experiments of all signals at a) 100 kHz b) 200 kHz c) 500 kHz.

further studied. Furthermore, theoretical models that correlate the slew rate, amplitude, and frequency of the variable magnetic field with generated heat must be developed.

On the other hand, the adjustments made to the previous design, like the *STM32F446RE* control chip, new four-pin Silicon-Carbide (SiC) MOSFETs, the capacitor bank the isolated power supplies, Schottky diodes, and all the changes made to the PCB design reduced oscillation and electromagnetic interference which resolved overheating problem mainly when operating at a frequency of 1 MHz.

The coil is required to generate a value of at least 10 mT up unto 30 mT, especially in future in Vitro studies, where the nanoparticle concentration cannot exceed 0.1 mg/mL or

less it will cause cell toxicity [38], [39]. Following the calculations in (5), the magnetic field generated at 60 A_{pk-pk} was 6.42 mT. Consequently, further improvements on the coil designs are necessary to improve the experimental apparatus further. However, since our experiments are limited to inert; hence no toxicity risks are taken, and on the other hand our objective is to validate our initial hypothesis that the lack of magnetic field was compensated by maximizing the nanoparticles concentration.

V. CONCLUSION

In this paper, the use of Full-Bridge inverters to generate high-frequency alternate magnetic fields for cancer treatment has been discussed. An inverter with SiC devices switched at a variable frequency and obtaining ZVS is proposed, making it adequate for the high-frequency application. Adjusting the phase-shift, different types of current shapes are obtained. Thanks to the use of SiC devices, switching frequencies up to 1 MHz have been reached at voltage levels as high as 200 V, which was unfeasible before, and forced these tests to be done with a power amplifier, which are bulky, expensive, and lossy. The prototype designed for this application was able to handle high currents under a wide range of frequencies. In addition, the prototype proved more efficient and power-dense than conventional power amplifiers used for this application.

Preliminary inert experiments were done at a similar nanoparticle concentration at an equal AMF intensity for the same period; the Square-Trapezoidal signal registered more than +2°C heat generation more than the sinusoidal signal Trapezoidal signal reported almost +1.5°C. These results proved the effectiveness of the slope of the AMF signal on the efficiency of hyperthermia and the power dissipation of the nanoparticles next to the frequency.

However, all the experiments in this study are made using 75 mg/ml nanoparticle concentration exclusively. Therefore, the next step will be to recreate the same experimental condition using lower concentration nanoparticles to demonstrate the contribution of AMF waveforms with more significant slopes in the nanoparticle concentration while maintaining or even increasing the nanoparticle's heat efficiency. This will lead to a decrease in the nanoparticle requirement in Magnetic hyperthermia significantly; hence, reducing cytotoxicity risks in in-Vitro and in-Vivo experiments [22], [23], [38].

Also, we aim to numerically demonstrate the heat dissipation caused by unconventional AMF signals, either by adjusting the Rosensweig model or using our approach.

As for the system, it is imperative to develop a new coil that would raise the magnetic field strength, allowing us to reach even higher current amplitudes than those obtained so far since we are using SiC MOSFETs that have pretty high current capabilities. The coil is made of custom-designed Litz wire, following our design specifications, optimizing it for high-frequency applications. Also, a cooling water system will be added, contributing even more to high-frequency high current dissipation.

As for the magnetic field intensity measurement of the new coil, although *Ansys Maxwell* simulations and theoretical calculations are quite reliable; yet, a suitable hall probe will be acquired for real-time magnetic field measurement.

All these upgrades will solve our current known limitations and allow us to go forward with inert experimentation, all the way to in Vitro and Vivo experiments.

ACKNOWLEDGMENT

The authors thank Maria del Puerto Morales for the donation of the nanoparticles. Milagros Ramos and Soledad Martinez for their assistance in the establishment of the experimental protocols. Also UPM Students M. Rivera, A. Miranda-Martínez, P. Sánchez, and D. Muñoz for their contribution in the system development. In addition, EPF-Montpellier student J. Sait and UPM students M. Rodriguez, L. Souiade, and J. Domingo for their support in the experimental phase. Michael Zeinoun thanks R. Jamil from Ac6-Paris for his support with the *STM32F446RE-Nucleo*. Some of the figures were created with BioRender.com.

REFERENCES

[1] P. Release, "Latest global cancer data: Cancer burden rises to 18.1 million new cases and 9.6 million cancer deaths in 2018," World Health Org., Int. Agency Res. Cancer, Lyon, France, Tech. Rep. 263, 2018, pp. 13–15.
[2] V. Hartwig, G. Giovannetti, N. Vanello, M. Lombardi, L. Landini, and S. Simi, "Biological effects and safety in magnetic resonance imaging: A review," *Int. J. Environ. Res. Public Health*, vol. 6, no. 6, pp. 1778–1798, Jun. 2009.
[3] M. Mahmoudi, S. Sant, B. Wang, S. Laurent, and T. Sen, "Superparamagnetic iron oxide nanoparticles (SPIONs): Development, surface modification and applications in chemotherapy," *Adv. Drug Del. Rev.*, vol. 63, nos. 1–2, pp. 24–46, Jan. 2011.
[4] A. E. Deatsch and B. A. Evans, "Heating efficiency in magnetic nanoparticle hyperthermia," *J. Magn. Magn. Mater.*, vol. 354, pp. 163–172, Mar. 2014.
[5] D. Chang, M. Lim, J. A. C. M. Goos, R. Qiao, Y. Y. Ng, F. M. Mansfeld, M. Jackson, T. P. Davis, and M. Kavallaris, "Biologically targeted magnetic hyperthermia: Potential and limitations," *Frontiers Pharmacol.*, vol. 9, P. 831, Aug. 2018.
[6] D. Mertz, O. Sandre, and S. Bégin-Colin, "Drug releasing nanoplatforms activated by alternating magnetic fields," *Biochimica et Biophysica Acta (BBA)-Gen. Subjects*, vol. 1861, no. 6, pp. 1617–1641, Jun. 2017.
[7] I. Rubia-Rodríguez *et al.*, "Whither magnetic hyperthermia? A tentative roadmap," *Materials*, vol. 14, no. 4, p. 706, Feb. 2021.
[8] M. Moros, "Triggering antitumoural drug release and gene expression by magnetic hyperthermia," *Adv. Drug Del. Rev.*, vol. 138, pp. 326–343, Jan. 2019.
[9] Y. Wang and D. S. Kohane, "External triggering and triggered targeting strategies for drug delivery," *Nature Rev. Mater.*, vol. 2, no. 6, p. 17020, Jun. 2017.
[10] S. Mura, J. Nicolas, and P. Couvreur, "Stimuli-responsive nanocarriers for drug delivery," *Nature Mater.*, vol. 12, no. 11, pp. 991–1003, Nov. 2013.
[11] *ClinicalTrials.gov Search Results 09/05/2018*, U.S. Nat. Library Med., Bethesda, MD, USA, 2018, Art. no. 2181075.
[12] D. Bobo, K. J. Robinson, J. Islam, K. J. Thurecht, and S. R. Corrie, "Nanoparticle-based medicines: A review of FDA-approved materials and clinical trials to date," *Pharmaceutical Res.*, vol. 33, no. 10, pp. 2373–2387, Jun. 2016.
[13] R. Mejías, S. Pérez-Yagüe, L. Gutiérrez, L. I. Cabrera, R. Spada, P. Acedo, C. J. Serna, F. J. Lázaro, Á. Villanueva, M. D. P. Morales, and D. F. Barber, "Dimercaptosuccinic acid-coated magnetite nanoparticles for magnetically guided *in vivo* delivery of interferon gamma for cancer immunotherapy," *Biomaterials*, vol. 32, no. 11, pp. 2938–2952, Apr. 2011.
[14] A. Jordan, R. Scholz, P. Wust, H. Fähling, and R. Felix, "Magnetic fluid hyperthermia (MFH): Cancer treatment with AC magnetic field induced excitation of biocompatible superparamagnetic nanoparticles," *J. Magn. Magn. Mater.*, vol. 201, nos. 1–3, pp. 413–419, 1999.

[15] N. Manuchehrabadi, Z. Gao, J. Zhang, H. L. Ring, Q. Shao, F. Liu, M. McDermott, A. Fok, Y. Rabin, K. G. M. Brockbank, M. Garwood, C. L. Haynes, and J. C. Bischof, "Improved tissue cryopreservation using inductive heating of magnetic nanoparticles," *Sci. Transl. Med.*, vol. 9, no. 379, Mar. 2017, Art. no. eaah4586.

[16] A. Espinosa, J. Kolosnjaj-Tabi, A. Abou-Hassan, A. P. Sangnier, A. Curcio, A. K. A. Silva, R. Di Corato, S. Neveu, T. Pellegrino, L. M. Liz-Marzán, and C. Wilhelm, "Magnetic (hyper) thermia or photothermia? Progressive comparison of iron oxide and gold nanoparticles heating in water, in cells, and *in vivo*," *Adv. Funct. Mater.*, vol. 28, no. 37, Jul. 2018, Art. no. 1803660.

[17] R. Di Corato, "Magnetic hyperthermia efficiency in the cellular environment for different nanoparticle designs," *Biomaterials*, vol. 35, no. 24, pp. 6400–6411, Aug. 2014.

[18] R. Mejías, P. H. Flores, M. Talelli, J. L. Tajada-Herráiz, M. E. F. Brollo, Y. Portilla, M. P. Morales, and D. F. Barber, "Cell-promoted nanoparticle aggregation decreases nanoparticle-induced hyperthermia under an alternating magnetic field independently of nanoparticle coating, core size, and subcellular localization," *ACS Appl. Mater. Interfaces*, vol. 11, no. 1, pp. 340–355, Jan. 2019.

[19] S. Del Sol-Fernández, Y. Portilla-Tundidor, L. Gutiérrez, O. F. Odio, E. Reguera, D. F. Barber, and M. P. Morales, "Flower-like Mn-doped magnetic nanoparticles functionalized with α_V β_3 integrin-ligand to efficiently induce intracellular heat after alternating magnetic field exposition, triggering glioma cell death," *ACS Appl. Mater. Interfaces*, vol. 11, no. 30, pp. 26648–26663, Jul. 2019.

[20] A. P. Sangnier, S. Preveral, A. Curcio, A. K. A. Silva, C. T. Lefèvre, D. Pignol, Y. Lalatonne, and C. Wilhelm, "Targeted thermal therapy with genetically engineered magnetite magnetosomesRGD: Photothermia is far more efficient than magnetic hyperthermia," *J. Controlled Release*, vol. 279, pp. 271–281, Jun. 2018.

[21] S. Suzuki and A. Satoh, "Influence of the cluster formation in a magnetic particle suspension on heat production effect in an alternating magnetic field," *Colloid Polym. Sci.*, vol. 297, no. 10, pp. 1265–1273, Oct. 2019.

[22] A. M. Rosales, E. Aznar, C. Coll, R. A. G. Mendoza, A. L. U. Bojorge, N. F. Gonzalez, R. Martinez-Manez, F. del Pozo Guerrero, and J. J. S. Olmedo, "Study of the dependency of the specific power absorption rate on several characteristics of the excitation magnetic signal when irradiating a SPION-containing ferrofluid," *J. Magn.*, vol. 21, no. 3, pp. 460–467, Sep. 2016.

[23] O. Garcia, N. Moreno-Arrones, A. B. Cuesta, A. Gutierrez, P. Alou, J. A. Oliver, J. A. Cobos, J. Uceda, E. Aznar, R. Martinez-Manez, C. Sanchez, O. E. Casanova, J. J. Serrano, and F. del Pozo, "Development and testing of a new instrument for researching on cancer treatment technologies based on magnetic hyperthermia," *IEEE J. Emerg. Sel. Topics Power Electron.*, vol. 4, no. 1, pp. 243–251, Mar. 2016.

[24] A. U. Bojorge, *Progress in the Development of a Device for Applications in Nanomedicine Through Magnetic Hyperthermia Therapy for Cancer Treatment*. Barcelona, Spain: Nanobioapp, 2015.

[25] M. Mohseni and A. Rajaei, "Design of alternating magnetic ELD generator for magnetic UID hyperthermia research application," *Sci. Iran.*, vol. 25, no. 6, pp. 3507–3516, 2018.

[26] L. Ibarra, H. Bastida, P. Ponce, and A. Molina, "Robust control for buck voltage converter under resistive and inductive varying load," in *Proc. 13th Int. Conf. Power Electron. (CIEP)*, Jun. 2016, pp. 126–131.

[27] J. A. Sabate, V. Vlatkovic, R. B. Ridley, F. C. Lee, and B. H. Cho, "Design considerations for high-voltage high-power full-bridge zero-voltage-switched PWM converter," in *Proc. 5th Annu. Proc. Appl. Power Electron. Conf. Exposit.*, 1990, pp. 275–284.

[28] G. Hua and F. C. Lee, "Soft-switching techniques in PWM converters," *IEEE Trans. Ind. Electron.*, vol. 42, no. 6, pp. 595–603, Dec. 1995.

[29] R. Watson and F. C. Lee, "A soft-switched, full-bridge boost converter employing an active-clamp circuit," in *Proc. 27th Annu. IEEE Power Electron. Specialists Conf. (PESC) Rec.*, vol. 2, Jun. 1996, pp. 1948–1954.

[30] U. R. Prasanna and A. K. Rathore, "Extended range ZVS active-clamped current-fed full-bridge isolated DC/DC converter for fuel cell applications: Analysis, design, and experimental results," *IEEE Trans. Ind. Electron.*, vol. 60, no. 7, pp. 2661–2672, Jul. 2013.

[31] R. Redl, N. O. Sokal, and L. Balogh, "A novel soft-switching full-bridge DC/DC converter: Analysis, design considerations, and experimental results at 1.5 kW, 100 kHz," *IEEE Trans. Power Electron.*, vol. 6, no. 3, pp. 408–418, Jul. 1991.

[32] Z. Dong, X. Wu, K. Sheng, and J. Zhang, "Impact of common source inductance on switching loss of SiC MOSFET," in *Proc. IEEE 2nd Int. Future Energy Electron. Conf. (IFEEC)*, Nov. 2015, pp. 1–5.

[33] N. Caka, M. Zabeli, M. Limani, and Q. Kabashi, "Influence of MOSFET parameters in its parasitic capacitance and their impact in digital circuits," *WSEAS Trans. Circuits Syst.*, vol. 6, no. 6, pp. 281–287, Mar. 2007.

[34] J. Dodge, "Eliminating parasitic oscillation between parallel MOSFETs," Adv. Power Technol., Appl. Note APT-0402 Rev. A, Mar. 2004. [Online]. Available: https://www.semanticscholar.org/paper/Eliminating-Parasitic-Oscillation-between-Parallel-Dodge/2d7d83fb60389e0e3907039c37cea031a1951197#citing-papers

[35] S. Dürr, W. Schmidt, C. Janko, H. P. Kraemer, P. Tripal, F. Eiermann, R. Tietze, S. Lyer, and C. Alexiou, "A novel magnetic field device for inducing hyperthermia using magnetic nanoparticles," *Biomed. Tech.*, vol. 58, no. SI-1-Track-E, 2013, Art. no. 000010151520134129, doi: 10.1515/bmt-2013-4129.

[36] M. M. Saari, M. A. H. P. Zaini, H. Ahmad, and N. A. C. Lah, "An AC magnetometer using automatic frequency switching of a resonant excitation coil for magnetic nanoparticles characterization," in *Proc. 9th IEEE Control Syst. Graduate Res. Colloq. (ICSGRC)*, Shah Alam, Malaysia, Aug. 2018, pp. 207–210.

[37] M. Kasper, R. M. Burkart, G. Deboy, and J. W. Kolar, "ZVS of power MOSFETs revisited," *IEEE Trans. Power Electron.*, vol. 31, no. 12, pp. 8063–8067, Dec. 2016, doi: 10.1109/TPEL.2016.2574998.

[38] A. G. Roca, L. Gutiérrez, H. Gavilán, M. E. Fortes Brollo, S. Veintemillas-Verdaguer, and M. D. P. Morales, "Design strategies for shape-controlled magnetic iron oxide nanoparticles," *Adv. Drug Del. Rev.*, vol. 138, pp. 68–104, Jan. 2019.

[39] J. Jose, R. Kumar, S. Harilal, G. E. Mathew, D. G. T. Parambi, A. Prabhu, M. S. Uddin, L. Aleya, H. Kim, and B. Mathew, "Magnetic nanoparticles for hyperthermia in cancer treatment: An emerging tool," *Environ. Sci. Pollut. Res.*, vol. 27, no. 16, pp. 19214–19225, Jun. 2020.

[40] R. E. Rosensweig, "Heating magnetic fluid with alternating magnetic field," *J. Magn. Magn. Mater.*, vol. 252, pp. 370–374, Nov. 2002.

[41] H. Sarnago, J. M. Burdio, and O. Lucia, "WBG semiconductor and capacitor technology evaluation for pulsed electroporation applications," in *Proc. IEEE Appl. Power Electron. Conf. Exposit. (APEC)*, Mar. 2019, pp. 708–712.

[42] H. Sarnago, J. M. Burdio, T. Garcia-Sanchez, L. Mir, and O. Lucia, "A versatile large-signal high-frequency arbitrary waveform generator using GaN devices," in *Proc. IEEE Appl. Power Electron. Conf. Exposit. (APEC)*, Mar. 2019, pp. 458–462.

[43] J. Millan, P. Godignon, X. Perpina, A. Perez-Tomas, and J. Rebollo, "A survey of wide bandgap power semiconductor devices," *IEEE Trans. Power Electron.*, vol. 29, no. 5, pp. 2155–2163, May 2014, doi: 10.1109/TPEL.2013.2268900.

[44] *IEEE Standard for Safety Levels with Respect to Human Exposure to Electric, Magnetic, and Electromagnetic Fields, 0 Hz to 300 GHz*, Standard IEEE Std C95.1-2019 (Revision IEEE Std C95.1-2005/ Inc. IEEE Std C95.1-2019/Cor 1-2019), Oct. 2019, pp. 1–312.

[45] R. Bosshard, J. Muhlethaler, J. W. Kolar, and I. Stevanovic, "Optimized magnetic design for inductive power transfer coils," in *Proc. 28th Annu. IEEE Appl. Power Electron. Conf. Exposit. (APEC)*, Mar. 2013, pp. 1812–1819.

[46] F. O. R. Limiting and E. To, "International commission on non-ionizing radiation protection ICNIRP guidelines for limiting exposure to time—Varying," *Health Phys.*, vol. 74, no. 4, pp. 494–522, 1999.

[47] International Commission on Non-Ionizing Radiation Protection, "Guidelines for limiting exposure to time-varying electric and magnetic fields (1 Hz TO 100 kHz)," *Health Phys.*, vol. 99, no. 6, pp. 818–836, 2010.

MICHAEL ZEINOUN (Member, IEEE) was born in Andaket, Lebanon, in 1991. He received the B.S. degree in biomedical technologies from Lebanese German University, Lebanon, in 2012, and the M.S. degree in electrical engineering-biomedical emphasis from the University of Balamand, Lebanon, in 2016. He is currently pursuing the Ph.D. degree with the Laboratory of Bioinstrumentation and Nanomedicine, Center for Biomedical Technology, Universidad Politécnica de Madrid, in 2017. His current research interests include nanomedical anti-cancer treatments, magnetic hyperthermia, optical hyperthermia, nano-robotics, DC to AC converters, alternating magnetic field generators, bioinstrumentation, biosensors, semiconductor materials technology, and sensor development.

DIEGO SERRANO (Member, IEEE) was born in Granda, Spain, in 1993. He received the B.S. degree in industrial electronic engineering from the Universidad de Granada (UGR), Granada, in 2015, and the master's and Ph.D. degrees in electronic engineering from the Universidad Politécnica de Madrid (UPM), Madrid, Spain, in 2016 and 2021, respectively. His current research interests include DC and AC conversions for photovoltaic applications, multilevel converters, and applications with GaN and SiC devices.

PABLO TEZANOS MEDINA received the B.S. degree in telecommunication technologies and services engineering specializing in electronic systems from the School of Telecommunications Engineering (ETSIT), Technical University of Madrid (UPM), Madrid, Spain, in 2020.

ÓSCAR GARCÍA (Member, IEEE) was born in Madrid, Spain, in 1968. He received the M.S. and Ph.D. degrees from the Universidad Politécnica de Madrid (UPM), Madrid, in 1992 and 1999, respectively. He is currently a Full Professor with UPM. He is also the Director of the ETSII-UPM. He has been involved in more than 80 research projects. He has authored or coauthored more than 200 technical papers in conferences and journals. He holds eight patents. He was a recipient of the UPM Faculty Research and Development Award for less than 35 years, in 2003, and the UPM Innovation in Education Award, in 2005.

MIROSLAV VASIĆ (Senior Member, IEEE) was born in Serbia, in 1981. He received the B.E. degree from the University of Belgrade, Belgrade, Serbia, in 2005, and the M.S. and Ph.D. degrees from the Universidad Politécnica de Madrid (UPM), Madrid, Spain, in 2007 and 2010, respectively. He is currently an Assistant Professor with UPM. He has advised two Ph.D. thesis. He has authored or coauthored more than 50 articles in the IEEE journals and conferences. He holds two patents. His areas of interests include DC-DC converters, power converters for R.F. applications, and converter topologies optimization. He received the SEMIKRON Innovation Award for the teamwork on "R.F. Power Amplifier with Increased Efficiency and Bandwidth," in 2012. In 2015, he received a Medal from the Spanish Royal Academy of Engineering for his research trajectory as a Young Researcher. In 2016, he received the Best Young Researcher Award from UPM. He has been cooperating with the IEEE and other professional associations as a reviewer and the session chair.

JOSÉ JAVIER SERRANO-OLMEDO received the degree and the Ph.D. degree in telecommunication engineering from the Universidad Politécnica de Madrid (UPM), in 1990 and 1996, respectively. He has been an Associate Professor at UPM, since 1998. He is the Principal Investigator of the Laboratory for Bioinstrumentation and Nanomedicine, Center for Biomedical Technology (LBN-CTB-UPM), a member of the Life Supporting Technology Group, and the Director and a member of the Networking Center for Biomedical Research on Bioengineering, Biomaterials, and Nanomedicine, Instituto de Salud Carlos III, Spain. He has been a supervisor of more than 15 Ph.D. students. He has authored or coauthored more than 100 papers, including articles and conference contributions, and participated in more than 30 research projects. He has four patents and is running three companies of technology base. His research interests include semiconductor materials technology and electronic technology for electronic instrumentation, sensor development, and networking, nanomedicine technologies, mainly using nanoparticles, the development of gravimetric biosensors and electromedicine systems, and accessible and assistive technologies based on serious games, virtual and augmented reality technology, human activity recognition, and human motion with inertial sensors.